ACS APPLIED ELECTRONIC MATERIALS

pubs.acs.org/acsaelm Article

Electronic and Optical Properties of Threading Dislocations in *n*-Type 4H-SiC

Hao Luo,[†] Jiajun Li,[†] Guang Yang, Ruzhong Zhu, Yiqiang Zhang, Rong Wang,* Deren Yang, and Xiaodong Pi*

Cite This: *ACS Appl. Electron. Mater.* 2022, 4, 1678−1683 Read Online

ACCESS | Metrics & More | Article Recommendations

ABSTRACT: Despite the decades of development of the single-crystal growth and homoepitaxy of 4H silicon carbide (4H-SiC), high-density threading dislocations (TDs) still remain in 4H-SiC. In this work, we show that the diameters, depths, and inclination angles of molten-alkali etched pits can be employed to discriminate threading edge dislocations (TEDs), threading screw dislocations (TSDs), and threading mixed dislocations (TMDs) in 4H-SiC. The formation of etch pits of TEDs, TSDs, and TMDs during molten-alkali etching is found to be assisted by the dislocation line, dislocation step, and successively dislocation line and step, respectively. By inspecting the surface potentials of *n*-type 4H-SiC with Kelvin probe force microscopy (KPFM), we show that both TSDs and TEDs behave as donors in *n*-type 4H-SiC, which gives rise to charge depletion at TDs in *n*-type 4H-SiC. TDs are found to participate in the broad band D1 luminescence of 4H-SiC, as evidenced by the fact that the microphotoluminescence (micro-PL) intensities at the centers of TDs are stronger than those in dislocation-free regions of 4H-SiC. Understandings gained in this work may help the optimization of *n*-type 4H-SiC by manipulating the electronic and optical properties of TDs.

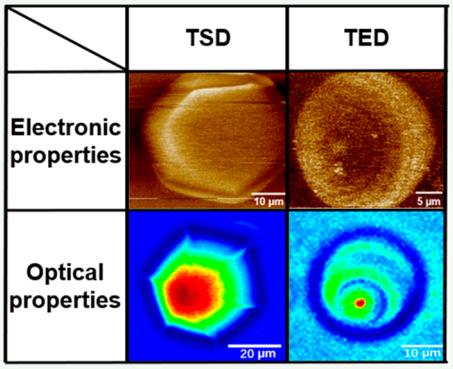

KEYWORDS: *4H-SiC, defects, dislocations, electronic properties, optical properties*

1. INTRODUCTION

Owning to the advantages of wide band gap, high breakdown electric field strength, high saturation drift velocity, and high thermal conductivity, 4H silicon carbide (4H-SiC) has been not only advancing the development of power electronics based on the homoepitaxy of 4H-SiC thin films but also promoting high-frequency electronics as ideal substrates for the heteroepitaxy of group-III nitrides.[1−4] The homoepitaxy of 4H-SiC thin films is carried out on *n*-type 4H-SiC substrates. Therefore, understanding the properties of dislocations in *n*-type 4H-SiC is important to understand the performance of 4H-SiC power devices. Despite the decades of development of the single-crystal growth and homoepitaxy of 4H-SiC, high-density threading dislocations (TDs) remain in 4H-SiC.[5,6] TDs usually originate from heterogeneous inclusions, silicon droplets, seed crystals, thermal stress, and mechanical stress.[7−9] TDs in 4H-SiC can be classified into threading edge dislocations (TEDs), threading screw dislocations (TSDs), threading mixed dislocations (TMDs), and micropipes (MPs), with the Burgers vectors of $(\langle 11{-}20\rangle a)/3$, $\pm c$, $c + a$, and $\pm nc$ (n = 3−10), respectively.[8,10,11] Nowadays the density of device-killing MPs is lowered down to ∼0.1 cm^{-2} in 4H-SiC substrates, while the densities of TEDs, TSDs, and TMDs remain in the order of magnitude of 10^3 −10^4 cm^{-2}.[12,13] TEDs and TSDs in 4H-SiC epitaxial layers are usually inherited from 4H-SiC substrates, and are found to increase the leakage current and premature breakdown of 4H-SiC-based power devices.[14−16] Furthermore, TDs in *n*-type 4H-SiC substrates act as the nucleation centers of stacking faults and basal plane dislocations (BPDs), which lead to the degradation of 4H-SiC-based bipolar devices.[17−19] Therefore, it is imperative to understand the basic properties of TDs in 4H-SiC, which may help the optimization of 4H-SiC by manipulating the properties of TDs.

Molten-alkali etching is usually adopted to reveal dislocations in 4H-SiC, which removes strained atoms surrounding TDs and forms etch pits at the surface of 4H-SiC.[20,21] Researchers have established an empirical approach to distinguish TSDs from TEDs by assuming that the average size of the etch pits for TSDs is 1.6−2.1 times larger than that of the etch pits for TEDs.[22] However, the shapes, densities,

Received: December 26, 2021
Accepted: March 28, 2022
Published: April 12, 2022

https://doi.org/10.1021/acsaelm.1c01330
ACS Appl. Electron. Mater. 2022, 4, 1678−1683

and sizes of molten-alkali etched pits significantly vary with the alkali species, etching duration, and doping concentration of 4H-SiC, makes it difficult to discriminate.[23−25] More significantly, both synchrotron X-ray-topography (XRT) and transmission-electron-microscopy (TEM) investigations have verified that TMDs are the dominant configurations of TSD/TMDs in 4H-SiC.[26,27] However, the morphology of the etch pits of TMDs is still ambiguous, which leads to difficulty in the statistics of the density of TMDs in 4H-SiC. In addition, it has been found that electrons tend to accumulate at TSDs,[28] while the electronic properties of TEDs are still not clear. Feng et al. found that the nonradiative recombination dominated the recombination of photogenerated carriers at TDs in 4H-SiC epilayers.[29] The photoluminescence (PL) of both TSDs and TEDs were observed around the wavelengths of 850 and 600 nm, respectively.[30] Ichikawa et al. pointed out that the intrinsic PL emission wavelength of TDs is in the infrared region of 700−950 nm.[31] Nagano et al. found that the intrinsic PL peaks of TSDs and TEDs appear at 800−950 nm and >950 nm, respectively.[32] However, the effect of TDs on the PL emission of the host 4H-SiC is still ambiguous. The electronic and optical properties of TMDs are induced by both TSDs and TEDs, which demands insightful understanding on the electronic and optical properties of TSDs and TEDs.

In this work, we show that TEDs, TSDs, and TMDs can be discriminated by combining the analyses of the diameters, depths, and inclination angles of the molten-alkali etched pits of 4H-SiC. By inspecting the surface potentials of *n*-type 4H-SiC with Kelvin probe force microscopy (KPFM), we find that TDs behave as donors in *n*-type 4H-SiC, resulting in the charge depletion at TDs in *n*-type 4H-SiC. It is found that both oxygen complexes and TDs participate in the broad band D1 luminescence of *n*-type 4H-SiC. The micro-PL intensities at the centers of TDs are stronger than those in dislocation-free regions, indicating that photogenerated carriers tend to recombine at TDs. Understanding gained in this work on the electronic and optical properties of TDs may help the optimization of *n*-type 4H-SiC by tailoring the electronic and optical properties of TDs.

2. EXPERIMENT METHODS

2.1. Sample Preparation. The *n*-type 4H-SiC boules were grown by the physical vapor transport (PVT) approach, with the growth temperature ranging from 2200 to 2300 °C. High-purity nitrogen gas (N_2) was mixed with argon (Ar) in the growth furnace to prepare *n*-type 4H-SiC. The pressure for the mixed gas of N_2 and Ar was maintained in the range 1−10 mbar during the growth of *n*-type 4H-SiC. The as-grown *n*-type 4H-SiC boules were then subsequently subjected to the 4.0° off-axis slicing, mechanical lapping, chemical mechanical polishing (CMP) and cleaning, and eventually resulted in *n*-type 4H-SiC substrates with the Si-face being treated by CMP. The N concentration in the *n*-type 4H-SiC is 1×10^{18} cm^{-3}. The 1 × 1 cm^2 samples were finally cut from the 4H-SiC substrates.

Before etching, the *n*-type 4H-SiC samples were ultrasonically cleaned with acetone, ethanol, and deionized water and then immersed in 10% hydrofluoric acid solution to remove the contamination and oxide on the surface. Molten-alkali etching of the *n*-type 4H-SiC samples was carried out in a Ni crucible, with the samples placed in Ni-wire meshes. The molten-KOH etching experiments were performed at 550 °C for 20 min. In order to better reveal dislocations, Na_2O_2 was adopted as the additive during KOH etching. The weight ratio of KOH:Na_2O_2 was 50:3. After the molten-alkali etching, the samples were cleaned by the same procedure before etching.

2.2. Characterization. Because the revealing of dislocations by molten-alkali etching is more prominent for the Si-face of 4H-SiC, we characterize the etch pits of dislocations at the Si-face of the etched 4H-SiC samples. The shapes and depth profiles of the etch pits were characterized by three-dimensional imaging using laser scanning confocal microscopy (LSCM) (ZEISS LSM900). The surface potentials of both the etch pits and perfect regions of *n*-type 4H-SiC were measured by the Kelvin probe force microscopy (KPFM) approach equipped in an atomic force microscope (AFM) (Bruker Electrical & Magnetic Lift modes) with a Pt−Ir coated Si cantilever (work function, 5.5 eV; resonant frequency, 75 kHz; spring constant, 3 N/m; lever thickness, 225 μm; lever width, 35 μm). PL spectra and micro-PL mapping were obtained using HORIBA LABRAM HR Evolution, which is capable of acquiring PL information by the full spectral scanning mode (acquiring the PL spectra) and a specified wavelength mode (acquiring micro-PL intensity mapping). The PL of the *n*-type 4H-SiC samples were excited by the 25 mW, 325 nm line of the He−Cd laser. The exposure time of the laser is set as 0.1 s.

3. RESULTS AND DISCUSSION

3.1. Correlation of Etch Pits and TDs. Figure 1(a) shows a representative optical microscope image displaying the surface morphology of the molten-KOH etched *n*-type 4H-SiC. Similar to previous researches, the molten-KOH etching results in hexagonal etch pits, which correspond to TDs in 4H-SiC.[22] We note that the etch pits deviate from the regular hexagon, as a result of the 4.0° off-axis slicing of the *n*-type 4H-SiC sample. According to the empirical approach, the larger pits and smaller pits correspond to TSDs and TEDs, respectively. However, the empirical approach cannot identify TMDs. The morphologies of the larger pits are classified to "Type-I" and "Type-II". It seems that the "Type-I" etch pit

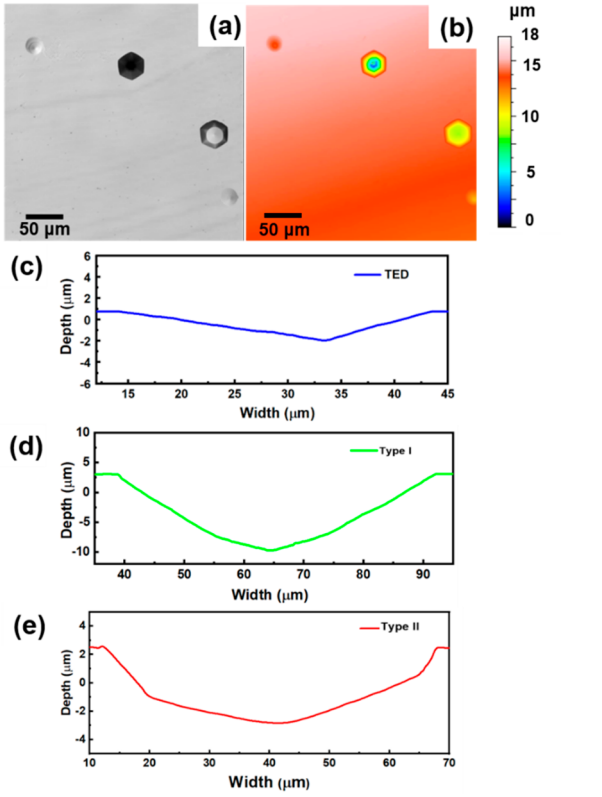

Figure 1. Representative (a) OM image and (b) LSCM image of the etched *n*-type 4H-SiC sample, as well as the depth profiles for the (c) etch pit of the TED, (d) "Type-I" etch pit, and (e) "Type-II" etch pit.

https://doi.org/10.1021/acsaelm.1c01330
ACS Appl. Electron. Mater. 2022, 4, 1678−1683

ends in a deeper point, and the "Type-II" etch pit ends in a deeper round plate. With the assistance of LSCM, we take the depth of the etch pits of TDs into account (Figure 1 (b)). Interestingly, there exist three kinds of depth profiles for the etch pits. As shown in Figure 1(c), the depth profiles of the smaller etch pits are gentle; they correspond to the etch pits of TEDs. The depth of the "Type-I" etch pit is more than 10 μm, and the slope is unitarily steep throughout the etch pit (Figure 1(d)). The depth of the "Type-II" etch pit is smaller than that of the "Type-I" etch pit. The depth profile of the "Type-II" etch pit can be divided into two parts. The slope for the deep center of the "Type-II" etch pit is relatively gentle, which is similar to that of TEDs. The slope of the outer fringe is steeper than that of the deep center, which is similar to those of TSDs (Figure 1(d)).

It is well-known that the strained atoms surrounding dislocations are more vulnerable to the attacking of OH^-. Upon molten-KOH etching, the surface strained atoms are removed from dislocations, which gives rise to the formation of etch pits at the surface of *n*-type 4H-SiC. TEDs in *n*-type 4H-SiC are formed by adding or removing an atomic plane along the [0001] direction. The strained atoms along the vertical dislocation line are removed during etching, which gives rise to the formation of smaller etch pits. The dislocation line assisted etching leads to the fact that the bottom of the etch pit of TED ends in a point (Figure 2(a)). TSDs with the Burgers vector of

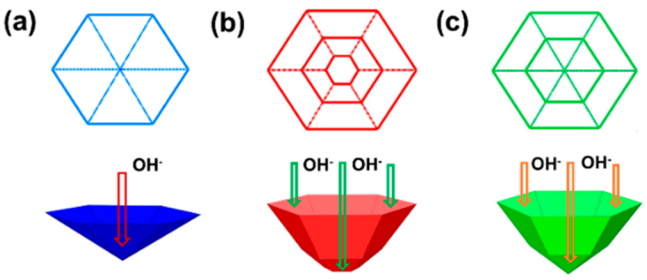

Figure 2. Schematic diagram showing the etching mechanism of the (a) TED, (b) TSD, and (c) TMD in 4H-SiC.

$\pm c$ are formed due to the spiral growth of *n*-type 4H-SiC and create steps when terminating at the surface of 4H-SiC. The molten-alkali etching process enlarges the surface step by removing the highly strained atoms and penetrates along the spiral dislocation step. The step-assisted etching mechanism gives rise to the larger each pit which ends by the circular plane (Figure 2(b)). The TMD is the mixture of the TSD and TED*a*. During the molten-KOH etching, the dislocation step assisted etching mechanism along the TSD is first activated. This gives rise to the larger etch pit of the TMD, as well as the steep slope of the outer fringe. As the etching process reaches the dislocation line of the TED-characterized dislocation, the dislocation line assisted etching mechanism along the TED is then activated, resulting in the gentle slope and terminal point of the center (Figure 2(c)). With the etching mechanism of TSDs and TMDs, we attribute the "Type-I" and "Type-II" etch pits to TSDs and TMDs, respectively. It should be noted that the stress fields around TDs, the etching mechanisms and thus the etch-pit morphologies of TDs in differently doped 4H-SiC are the same. Furthermore, the similar etching mechanisms and etch-pit morphologies of TDs also apply to other hexagonal polymorphs of SiC, such as 2H and 6H-SiC, due to the similar strain fields around the dislocations and crystal symmetry of the host. Given the Burger vector of TMDs being the mixture of those of TSDs and TEDs, the properties of TMDs are a mixture of those of TSDs and TEDs. Therefore, we then investigate the electronic and optical properties of representative TSDs and TEDs in *n*-type 4H-SiC.

3.2. Electronic Properties of TDs. The electronic properties of TSDs and TEDs are analyzed by detecting the contact potential difference (CPD) between the tip and the etched *n*-type 4H-SiC by the KPFM approach. The value of V_{CPD} is defined by[33]

$$V_{CPD} = \frac{\Phi_{sample} - \Phi_{tip}}{q} \quad (1)$$

where Φ_{sample} and Φ_{tip} are the work functions of the Pt−Ir coated tip and the sample, respectively, and q is the electronic charge. Therefore, KPFM is capable of imaging the local work function and, thus, the local Fermi energy of semiconductors. Figure 3(a) and (b) displays the surface potential mapping of

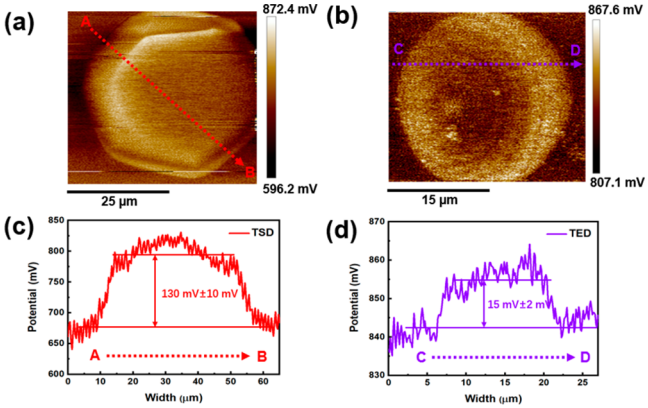

Figure 3. Surface potential mapping images of containing the etch pit of (a) TSD and (b) TED. Line profiles for the surface potentials across the etch pit of the TSD and TED are shown in parts (c) and (d), respectively.

the representative TSD and TED in *n*-type 4H-SiC, respectively. It is clear that the surface potentials for the etch pits of the TDs are higher than that of the dislocation-free region. By plotting the line profiles of the surface potentials, we find that the surface potentials of TSDs and TEDs are higher than the perfect region by 130 mV and 15 mV, respectively (Figure 3(c) and (d)). According to eq 1, the local work functions of TSDs and TEDs are lower than that of the perfect region of *n*-type 4H-SiC. Therefore, the nominally "local Fermi energies" of TSDs and TEDs are higher than that of the perfect region. That is to say, TSDs and TEDs both create donor states in *n*-type 4H-SiC with the N-doping concentration of 1×10^{18} cm^{-3}, which increases the local Fermi energies around them.

The positions of the donor states of TSDs and TEDs are then calculated by

$$\Phi = \chi + (E_C - E_F) \quad (2)$$

where χ is the electron affinity of 4H-SiC (3.8 eV) and E_C and E_F are the energies of the conduction band minimum and Fermi level, respectively. The measured surface potential of the tip is higher than that of the Au tip by 400 mV, with the standard work function of Au being 5.2 eV. With eqs 1 and 2, we find that the local Fermi energies of TSDs and TEDs are

https://doi.org/10.1021/acsaelm.1c01330
ACS Appl. Electron. Mater. 2022, 4, 1678−1683

pinned at the positions of 0.33 eV and 0.78 eV under the conduction band minimum (CBM) of *n*-type 4H-SiC, respectively. Huang et al. found that the local work function decreases in the order of defect-free region, TSD, and TED, indicating that TDs behave as acceptors in 4H-SiC epitaxial layers with the N concentration of 1×10^{16} cm^{-3}.[34] The different electronic properties of TDs may be attributed to the different N concentrations in 4H-SiC samples. In our recent work, we find that positively charged N dopants tend to accumulate at the core of BPDs in *n*-type 4H-SiC and contribute to the donor-like behavior of BPDs in *n*-type 4H-SiC.[35] Similarly, the donor-like behavior of TDs in *n*-type 4H-SiC could be originated by the accumulation of N dopants at the core of TDs. The local donor-like states of TDs lower the local conduction band of TDs in *n*-type 4H-SiC and pave the way for analyzing the electron transport mechanism and reliability of 4H-SiC power devices.

3.3. Optical Properties of TDs. The PL spectra of the perfect region of *n*-type 4H-SiC is first measured. We first measure the PL spectra of the perfect region of *n*-type 4H-SiC. As shown in Figure 4(a), the band-edge emission around 390 nm and the broad defect-related emission ranging from 450 to 750 nm are found for the *n*-type 4H-SiC substrate, which agree well with previous researches.[36,37] The broad band emission is the so-called D1 luminescence band of 4H-SiC, which was attributed to the surface oxides of 4H-SiC.[38] Due to the indirect band gap of 4H-SiC, the PL intensity of the band-edge emission is similar to that of D1 luminescence. The micro-PL spectra at the centers of the etch pits of TDs are then measured. It turns out that the emission peaks at the centers of TDs are similar to that of the perfect *n*-type 4H-SiC surface.

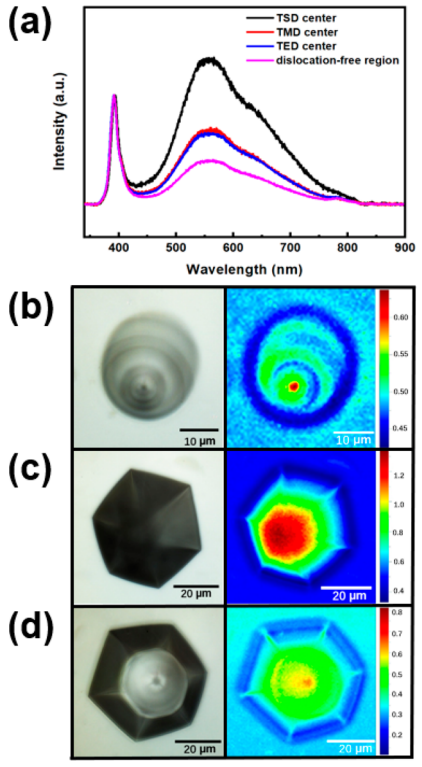

Figure 4. (a) Micro-PL spectra collected at the centers of TED, TSD, and TMD, as well as that collected at the dislocation-free region of centers 4H-SiC. OM images and micro-PL intensity mapping images of TED, TSD, and TMD are shown in parts (b), (c), and (d), respectively.

By normalizing the intensities of band-edge-emission peaks, we find that the PL intensities for the D1-luminescence centers of the TDs are all higher than that of the dislocation-free region of *n*-type 4H-SiC (Figure 4(a)). For the TED, the PL intensity inside the etch pit is stronger than that of the surface. The PL intensity is the strongest at the center of the etch pit, where the dislocation line of TED appears (Figure 4(b)). The PL intensity inside the etch pit of the TSD is also stronger than that of the surface, with the circular bottom emitting the strongest D1 luminescence (Figure 4(c)). For the TMD, which is composed of the TED-characterized center and the TSD-characterized outer fringe, the PL intensity decreases in the order of TED-characterized center, TSD-characterized outer fringe, and dislocation-free surface (Figure 4(d)). This indicates that even in *n*-type 4H-SiC substrates with relatively short carrier lifetime, the radiative recombination at the centers of TDs is stronger than that at the dislocation-free region. The enhanced D1 luminescence of TDs in *n*-type 4H-SiC indicates that the identification and statistics of TDs can be realized by wafer mapping of the PL intensity of the D1 luminescence.

Based on the above results, we analyze the radiative recombination at TDs in 4H-SiC. Due to the attacking of OH^- species, the oxygen complex, which is the primary candidate of the D1 luminescence, is the dominating surface state of the etched 4H-SiC samples. The oxygen complexes create continuum defect states both under the CBM and above the valence band maximum (VBM) of 4H-SiC ["TD-free" in Figure 5].[37] According to the etching mechanism of TDs, the bottoms of the etch pits of TEDs, TSDs, and TMDs are ended by the dislocation line of TED, the spiral dislocation step of TSD, and the dislocation line of TED, respectively. Similar to what happens in gallium nitrides, TDs introduce occupied defect levels above the VBM and unoccupied defect states under the CBM of 4H-SiC.[28,39] As evidenced by surface potential measurements, the local Fermi energies of TDs are higher than the dislocation-free region, indicating that the positions of the defect states of TDs are higher than that of the

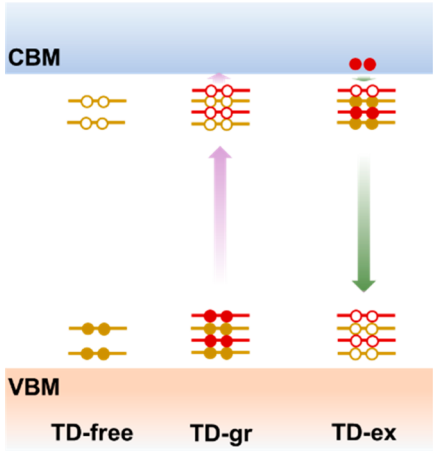

Figure 5. Schematic diagram showing the defect states of the dislocation-free region (TD-free), ground state of the TD (TD-gr), and excited state of the TD (TD-ex) of 4H-SiC. The dark yellow and red lines represent the defect states of oxygen complexes and TDs, respectively. The closed and open circles represent electrons and holes, respectively.

https://doi.org/10.1021/acsaelm.1c01330
ACS Appl. Electron. Mater. 2022, 4, 1678−1683

dislocation-free region. Therefore, the ground state for defects in 4H-SiC is featured by the occupied defect level above the VBM and the unoccupied defect level under the CBM, which is caused by the surface states of oxygen complexes and the defect states of TDs ("TD-gr" in Figure 5). Upon UV irradiation, electrons are excited to the CBM of 4H-SiC, which leaves holes in the VBM and the original occupied level of TDs ("TD-ex" in Figure 5). The electron−hole recombinations mediated by TDs are illustrated in Figure 5. Photoexcited electrons first relax to the unoccupied TD states under the CBM and then recombine with holes at the TD state above the VBM. The electron−hole recombination gives rise to the enhanced D1 luminescence around TDs in *n*-type 4H-SiC.

4. CONCLUSIONS

In conclusion, we have systematically explored the etching mechanism, electronic properties, and optical properties of TDs in 4H-SiC. By discriminating TEDs, TSDs, and TMDs through the analysis of the diameters, depths, and inclination angles of molten-KOH etched pits, we have clarified that the etching of TEDs, TSDs, and TMDs is assisted by dislocation lines, dislocation steps, and successively dislocation line and step, respectively. TSDs and TEDs introduce donor levels at E_c − 0.11 eV and E_c − 0.06 eV in *n*-type 4H-SiC, respectively. We also find that photogenerated carriers tend to recombine at TDs. Both TDs and oxygen complexes give rise to the broad band D1 luminescence in 4H-SiC, because micro-PL intensities at the centers of TDs are stronger than those in dislocation-free regions. Based on the understanding of the electronic and optical properties of TDs, we propose the two-stage recombination process mediated by TDs and oxygen complexes in 4H-SiC. Our work sheds light on tailoring the properties of 4H-SiC by tuning the electronic and optical properties of TDs.

AUTHOR INFORMATION

Corresponding Authors

Rong Wang − *State Key Laboratory of Silicon Materials and School of Materials Science and Engineering, Zhejiang University, Hangzhou 310027, China; Institute of Advanced Semiconductors & Zhejiang Provincial Key Laboratory of Power Semiconductor Materials and Devices, Hangzhou Innovation Center, Zhejiang University, Hangzhou, Zhejiang 311200, China;* orcid.org/0000-0003-3333-0180; Email: rong_wang@zju.edu.cn

Xiaodong Pi − *State Key Laboratory of Silicon Materials and School of Materials Science and Engineering, Zhejiang University, Hangzhou 310027, China; Institute of Advanced Semiconductors & Zhejiang Provincial Key Laboratory of Power Semiconductor Materials and Devices, Hangzhou Innovation Center, Zhejiang University, Hangzhou, Zhejiang 311200, China;* orcid.org/0000-0002-4233-6181; Email: xdpi@zju.edu.cn

Authors

Hao Luo − *State Key Laboratory of Silicon Materials and School of Materials Science and Engineering, Zhejiang University, Hangzhou 310027, China; Institute of Advanced Semiconductors & Zhejiang Provincial Key Laboratory of Power Semiconductor Materials and Devices, Hangzhou Innovation Center, Zhejiang University, Hangzhou, Zhejiang 311200, China;* orcid.org/0000-0002-7105-1943

Jiajun Li − *State Key Laboratory of Silicon Materials and School of Materials Science and Engineering, Zhejiang University, Hangzhou 310027, China; Institute of Advanced Semiconductors & Zhejiang Provincial Key Laboratory of Power Semiconductor Materials and Devices, Hangzhou Innovation Center, Zhejiang University, Hangzhou, Zhejiang 311200, China*

Guang Yang − *Key Laboratory of Optical Field Manipulation of Zhejiang Province, Zhejiang Sci-Tech University, Hangzhou 310018, China*

Ruzhong Zhu − *Institute of Advanced Semiconductors & Zhejiang Provincial Key Laboratory of Power Semiconductor Materials and Devices, Hangzhou Innovation Center, Zhejiang University, Hangzhou, Zhejiang 311200, China*

Yiqiang Zhang − *School of Materials Science and Engineering & Henan Institute of Advanced Technology, Zhengzhou University, Zhengzhou, Henan 450001, China;* orcid.org/0000-0002-2437-925X

Deren Yang − *State Key Laboratory of Silicon Materials and School of Materials Science and Engineering, Zhejiang University, Hangzhou 310027, China; Institute of Advanced Semiconductors & Zhejiang Provincial Key Laboratory of Power Semiconductor Materials and Devices, Hangzhou Innovation Center, Zhejiang University, Hangzhou, Zhejiang 311200, China*

Complete contact information is available at: https://pubs.acs.org/10.1021/acsaelm.1c01330

Author Contributions

†H.L. and J.J.L. contributed equally to this work.

Notes

The authors declare no competing financial interest.

ACKNOWLEDGMENTS

This work is supported by Pioneer and Leading Goose R&D Program of Zhejiang (Grant No. 2022C01021), National Key Research and Development Program of China (Grant No. 2018YFB2200101), Natural Science Foundation of China (Grant Nos. 91964107, 61774133), Fundamental Research Funds for the Central Universities (Grant No. 2018XZZX003-02), Natural Science Foundation of China for Innovative Research Groups (Grant No. 61721005), and Zhejiang University Education Foundation Global Partnership Fund.

REFERENCES

(1) She, X.; Huang, A. Q.; Lucía, Ó.; Ozpineci, B. Review of Silicon Carbide Power Devices and Their Applications. *IEEE Trans. Ind. Electron.* **2017**, *64* (10), 8193−8205.

(2) Pengelly, R. S.; Wood, S. M.; Milligan, J. W.; Sheppard, S. T.; Pribble, W. L. A Review of GaN on 4H-SiC High Electron-mobility Power Transistors and MMICs. *IEEE Trans. Microw. Theory Techn. Electron.* **2012**, *60* (6), 1764−1783.

(3) Powell, A. R.; Rowland, L. B. 4H-SiC Materials-progress, Status, and Potential Roadblocks. *Proc. IEEE* **2002**, *90* (9), 942−955.

(4) Kimoto, T.; Cooper, J. A. *Fundamentals of Silicon Carbide Technology: Growth, Characterization, Devices and Applications*; John Wiley & Sons: Singapore, 2014; DOI: 10.1002/9781118313534.

(5) Kimoto, T.; Watanabe, H. Defect Engineering in 4H-SiC Technology for High-voltage Power Devices. *Appl. Phys. Express* **2020**, *13* (12), 120101.

(6) Wellmann, P. J. Review of 4H-SiC Crystal Growth Technology. *Semicond. Sci. Technol.* **2018**, *33* (10), 103001.

(7) Dudley, M.; Huang, X. R.; Huang, W.; Powell, A. The mechanism of Micropipe Nucleation at Inclusions in Silicon Carbide. *Appl. Phys. Lett.* **1999**, *75* (6), 784−786.
(8) Ohtani, N.; Katsuno, M.; Tsuge, H.; Fujimoto, T.; Nakabayashi, M.; Yashiro, H.; Sawamura, M.; Aigo, T.; Hoshino, T. Propagation Behavior of Threading Dislocations During Physical Vapor Transport Growth of Silicon Carbide (4H-SiC) Single Crystals. *J. Cryst. Growth* **2006**, *286* (1), 55−60.
(9) Basceri, C.; Khlebnikov, I.; Khlebnikov, Y.; Muzykov, P.; Sharma, M.; Stratiy, G.; Silan, M.; Balkas, C. M. Growth of Micropipe-Free Single Crystal Silicon Carbide (SiC) Ingots Via Physical Vapor Transport (PVT). *Mater. Sci. Forum* **2006**, *527*, 39−42.
(10) Heindl, J.; Dorsch, W.; Strunk, H. P.; Müller, St. G.; Eckstein, R.; Hofmann, D.; Winnacker, A. Dislocation Content of Micropipes in 4H-SiC. *Phys. Rev. Lett.* **1998**, *80* (4), 740−741.
(11) Ohno, T.; Yamaguchi, H.; Kuroda, S.; Kojima, K.; Suzuki, T.; Arai, K. Direct Observation of Dislocations Propagated from 4H−4H-SiC Substrate to Epitaxial Layer by X-ray Topography. *J. Cryst. Growth* **2004**, *260* (1−2), 209−216.
(12) Neudeck, P. G.; Powell, J. A. Performance Limiting Micropipe Defects in Silicon Carbide Wafers. *IEEE. Electron. Device. Lett.* **1994**, *15* (2), 63−65.
(13) Hoshino, N.; Kamata, I.; Kanda, T.; Tokuda, Y.; Kuno, H.; Tsuchida, H. Reduction in Dislocation Densities in 4H-SiC Bulk Crystal Grown at High Growth Rate by High-temperature Gas-source Method. *Appl. Phys. Express* **2020**, *13* (9), 095502.
(14) Grekov, A.; Zhang, Q.; Fatima, H.; Agarwal, A.; Sudarshan, T. Effect of Crystallographic Defects on The Reverse Performance of 4H-SiC JBS Diodes. *Microelectron Reliab.* **2008**, *48* (10), 1664−1668.
(15) Maximenko, S. *Investigation of Device Performance Limiting Defects in Silicon Carbide Semiconductor*. University of South Carolina, 2005.
(16) Neudeck, P. G.; Huang, W.; Dudley, M. Study of Bulk and Elementary Screw Dislocation Assisted Reverse Breakdown in Low-voltage (<250 V) 4H-SiC p+n Junction Diodes-Part I: DC Properties. *IEEE Trans. Electron Devices* **1999**, *46* (3), 478−484.
(17) Ha, S.; Chung, H. J.; Nuhfer, N. T.; Skowronski, M. Dislocation Nucleation in 4H Silicon Carbide Epitaxy. *J. Cryst. Growth* **2004**, *262* (1−4), 130−138.
(18) Ha, S.; Benamara, M.; Skowronski, M.; Lendenmann, H. Core Structure and Properties of Partial Dislocations in Silicon Carbide p-i-n Diodes. *Appl. Phys. Lett.* **2003**, *83* (24), 4957−4959.
(19) Abadier, M.; Myers-Ward, R. L.; Mahadik, N. A.; Stahlbush, R. E.; Wheeler, V. D.; Nyakiti, L. O.; Eddy, C. R.; Gaskill, D. K.; Song, H.; Sudarshan, T. S. Nucleation of In-grown Stacking Faults and Dislocation Half-loops in 4H-SiC Epitaxy. *J. Appl. Phys.* **2013**, *114* (12), 123502.
(20) Dong, L.; Zheng, L.; Liu, X. F.; Zhang, F.; Yan, G. G.; Li, X. G.; Sun, G. S.; Wang, Z. G. Defect Revelation and Evaluation of 4H Silicon Carbide by Optimized Molten KOH Etching Method. *Mater. Sci. Forum* **2013**, *740*, 243.
(21) Cui, Y.; Hu, X.; Xie, X.; Xu, X. Threading Dislocation Classification for 4H-SiC Substrates Using The KOH Etching Method. *CrystEngComm.* **2018**, *20* (7), 978−982.
(22) Yao, Y. Z.; Ishikawa, Y.; Sugawara, Y.; Saitoh, H.; Shibata, N. Molten KOH Etching with Na_2O_2 Additive for Dislocation Revelation in 4H-SiC Epilayers and Substrates. *Jpn. J. Appl. Phys.* **2011**, *50* (7), 075502.
(23) Syväjärvi, M.; Yakimova, R.; Janzén, E. Anisotropic Etching of 4H-SiC. *J. Electrochem. Soc.* **2000**, *147* (9), 3519−3522.
(24) Zhuang, D.; Edgar, J. H. Wet Etching of GaN, AlN, and 4H-SiC: a review. *Mater. Sci. Eng. R.* **2005**, *48* (1), 1−46.
(25) Gao, Y.; Zhang, Z.; Bondokov, R.; Soloviev, S.; Sudarshan, T. The Effect of Doping Concentration and Conductivity Type on Preferential Etching of 4H-SiC by Molten KOH. *MRS Proceedings* **2004**, *815*, 139−143.
(26) Nakamura, D.; Yamaguchi, S.; Gunjishima, I.; Hirose, Y.; Kimoto, T. Topographic Study of Dislocation Structure in Hexagonal SiC Single Crystals with Low Dislocation Density. *J. Cryst. Growth* **2007**, *304* (1), 57−63.
(27) Konishi, K.; Nakamura, Y.; Nagae, A.; Kawabata, N.; Tanaka, T.; Tomita, N.; Watanabe, H.; Tomohisa, S.; Miura, N. Direct Observation and Three Dimensional Structural Analysis for Threading Mixed Dislocation Inducing Current Leakage in 4H-SiC IGBT. *Jpn. J. Appl. Phys.* **2020**, *59* (1), 011001.
(28) Chung, S.; Berechman, R. A.; McCartney, M. R.; Skowronski, M. Electronic Structure Analysis of Threading Screw Dislocations in 4H-SiC Using Electron Holography. *J. Appl. Phys.* **2011**, *109* (3), 034906.
(29) Feng, G.; Suda, J.; Kimoto, T. Nonradiative Recombination at Threading Dislocations in 4H-SiC Epilayers Studied by Micro-photoluminescence Mapping. *J. Appl. Phys.* **2011**, *110* (3), 033525.
(30) Liu, K. X.; Zhang, X.; Stahlbush, R. E.; Skowronski, M.; Caldwell, J. D. Differences in Emission Spectra of Dislocations in 4H-SiC Epitaxial Layers. *Mater. Sci. Forum* **2008**, *600*, 345.
(31) Ichikawa, S.; Kawahara, K.; Suda, J.; Kimoto, T. Carrier Recombination in n-Type 4H-SiC Epilayers with Long Carrier Lifetimes. *Appl. Phys. Express* **2012**, *5* (10), 101301.
(32) Nagano, M.; Kamata, I.; Tsuchida, H. Plan-View and Cross-Sectional Photoluminescence Imaging Analyses of Threading Dislocations in 4H-SiC Epilayers. *Jpn. J. Appl. Phys.* **2013**, *52* (4), 04CP09.
(33) Kim, H. K.; Kim, S. I.; Kim, S.; Lee, N. S.; Shin, H. K.; Lee, C. W. Relation Between Work Function and Structural Properties of Triangular Defects in 4H-SiC Epitaxial Layer: Kelvin Probe Force Microscopic and Spectroscopic Analyses. *Nanoscale* **2020**, *12* (15), 8216−8229.
(34) Huang, J. R.; Chen, T. W.; Lee, J. W.; Huang, C. F.; Hong, L. S. A Perspective on Leakage Current Induced by Threading Dislocations in 4H-SiC Schottky Barrier Diodes. *Mater. Lett.* **2022**, *310* (1), 131506.
(35) Li, J. J.; Wang, R.; Luo, H.; Yang, G.; Zhang, Y. Q.; Yang, D. R.; Pi, X. D. Nitrogen Decoration of Basal Plane Dislocations in 4H-SiC. *arXiv* **2022**, 2202.13508.
(36) Kawahara, C.; Suda, J.; Kimoto, T. Identification of Dislocations in 4H-SiC Epitaxial Layers and Substrates Using Photoluminescence Imaging. *Jpn. J. Appl. Phys.* **2014**, *53* (2), 020304.
(37) Torchynska, T. V.; Cano, A. D.; Sandoval, S. J.; Dybic, M.; Ostapenko, S.; Mynbaeva, M. Photoluminescence and Raman Spectroscopy in Porous 4H-SiC. *Microelectron. J.* **2005**, *36* (3), 536−538.
(38) Lu, W. F.; Tarekegne, A. T.; Ou, Y.; Kamiyama, S.; Ou, H. Temperature-dependent Photoluminescence Properties of Porous Fluorescent SiC. *Sci. Rep.* **2019**, *9* (1), 16333.
(39) Wang, R.; Tong, X.; Xu, J. X.; Dong, C. L.; Tan, W. Acceptor Decoration of Threading Dislocations in (Al,Ga)N/GaN Heterostructures. *Phys. Rev. Appl.* **2020**, *14* (2), 024039.

https://doi.org/10.1021/acsaelm.1c01330
ACS Appl. Electron. Mater. 2022, 4, 1678−1683